Load Current Decoupling Based LQ Control for Three-Phase Inverter

Xiangjun Quan, *Student Member, IEEE*, Zaijun Wu, Xiaobo Dou, Minqiang Hu, and Alex Q. Huang, *Fellow, IEEE*

***Abstract*—In classical inverter control, load current (disturbance) decoupling control is often used to improve the control performance. Yet, in a recent state-space control structure for multiresonant controllers, the load current decoupling technique is less studied. Moreover, in the classical control, the load current decoupling only has one control degree of freedom. Therefore, in this paper, a load current decoupling control combed linear quadratic (LQ) regulation is investigated, the proposed control structure that manipulates α and β axes as a unified system is adopted to increase the control degree of freedom. The LQ control synthesizes the state feedback control law including gains of the resonant controllers. Two general criteria, namely H_∞ norm and zero dynamic, are proposed as the design guideline for the load current decoupling control. The effectiveness and robustness of the proposed approach are validated through MATLAB/Simulink simulations and experiments with a 5-kVA testbed. The results prove that some favorable performances, for example, the fast recovering time, the small voltage drop, and the low total harmonic distortion, are achieved by the proposed approach compared to the classical dual-loop proportional-resonant (PR) control with load current decoupling and the optimal H_∞ control.**

***Index Terms*—Inverter control, linear quadratic (LQ) control, load current decoupling, linear matrix inequality (LMI).**

NOMENCLATURE

$\boldsymbol{A}_p$, $\boldsymbol{B}_{p1}$, $\boldsymbol{B}_{p2}$, $\boldsymbol{C}_p$	Continuous-time state-space description of three-phase inverters.
$\boldsymbol{A}_{dp}$, $\boldsymbol{B}_{dp1}$, $\boldsymbol{B}_{dp2}$, $\boldsymbol{C}_p$	Discrete-time state-space description of three-phase inverters.
θ	State variable of the digital control delay.
T_s	Sampling/switching period.
ω	Fundamental angle frequency: 100π rad/s
$\boldsymbol{A}$, $\boldsymbol{B}_1$, $\boldsymbol{B}_2$, $\boldsymbol{R}_r$, $\boldsymbol{C}$	Discrete-time state-space description of the augmented state-space model for the control system.
J	Linear quadratic index of the control system.
$\boldsymbol{Q}$, $\boldsymbol{R}$	Weight matrixes of the linear quadratic index.
$\boldsymbol{Q}_0$	Low bound of $\boldsymbol{Q}$.
Trace()	Trace of a matrix.
$D(q, r)$	The circle with the radius of r at center q.
'$\wedge$'	Solution of optimization problems.
$\|\|\cdot\|\|_2$, $\|\|\cdot\|\|_\infty$	2-norm and ∞-norm, respectively.
L_2	Time-domain 2-norm.
H_∞	Frequency-domain ∞-norm.
γ	Supremum of H_∞.
T_{wy}	Disturbance-output transfer function, namely output impedance.
$\boldsymbol{K}$	State feedback control law.
$\boldsymbol{K}_\mathrm{d}$	Load current decoupling law.

Manuscript received April 7, 2017; revised June 13, 2017; accepted July 28, 2017. Date of publication August 11, 2017; date of current version February 22, 2018. Recommended for publication by Associate Editor Dr. B. Lehman. This work was supported in part by the National Key Research and Development Program of China (2016YFB0900500), and in part by the State Key Laboratory of Smart Grid Protection and Control, SKL of SGPC, China. *(Corresponding author: Zaijun Wu.)*

X. Quan, Z. Wu, X. Dou, and M. Hu are with the Department of Electrical Engineering, Southeast University, Nanjing 210018, China (e-mail: qxj@seu.edu.cn; zjwu@seu.edu.cn; dxb_2001@sina.com; mqhu@seu.edu.cn).

A. Q. Huang is with the University of Texas at Austin, Austin, TX 78712 USA (e-mail: aqhuang@utexas.edu).

Color versions of one or more of the figures in this paper are available online at http://ieeexplore.ieee.org.

Digital Object Identifier 10.1109/TPEL.2017.2738021

I. INTRODUCTION

WHEN distributed energy resources (DERs) are integrated into microgrid (MG) systems, inverters serve as the power electronic interface device of the DERs. A lot of efforts have been dedicated to the control of MG inverters [1], [2]. In MG, the voltage-controlled inverters are generally designed to feed the critical loads. The performance of voltage-controlled inverters is usually assessed in terms of a set of dynamic-/steady-state indices, such as the voltage drop, recovering time under load variation, and the total harmonic distortion (THD) of the output voltage when feeding linear or nonlinear loads. To improve the aforementioned performance indices, many control algorithms have been proposed in the literatures.

Most early control algorithms are based on transfer function models. Those control methods are either multiloop control [3]–[6] or single-loop control [7], [8] and are widely employed today. The control gains are designed through the frequency-domain analysis. Adding load current decoupling control to classical multiloop controls can improve the dynamic performance. This has the advantage of designing control parameters with clear physical significance.

Compared to the transfer function model based classical method, the state-space model is more suitable for processing the multiple-input multiple-output (MIMO) system and performing quantified optimization, e.g., the linear quadratic (LQ) control. With the application of the state-space model, the load current is used in [9] and [10] to predict the output voltage leading to a model predictive control technique for

uninterruptible-power-supply (UPS) applications, but the simulation and experimental results reported in those two literatures fell short in minimizing THD compared to other referred literatures, for example, [11] and [12]. In [11] and [12], the load current is employed to compensate the uncertainties for an adaptive voltage control [11] and optimal voltage control [12]. In another adaptive voltage control [13], the load current is treated as a state variable. Those methods achieve good performance, such as low THD and fast response. The extended Lyapunov-function-based control in [14] designs a specific control law to ensure the global stability of the closed-loop system. The load current is also used in the control laws to satisfy the requirement of negative definite time derivative for the inverter system. It is worth noting that in those approaches [9]–[14], another critical function of the load current is to reduce the steady-state error of the output voltage. Usually, in those methods where the internal model principle (IMP) is absent, the control law should be designed carefully to achieve the zero steady-state error. Again, the load current feedforward is always indispensable.

A feedback linearization control is proposed in [15]. The control objective is linearized to be two cascaded integrators. It provides good results, such as low THD and high dynamic response. The major disadvantage of this technique is its weakness in parameter uncertainties. The differential flatness representation based on the capacitor energy for the inverter is proposed to achieve flatness-based control [16]. An integrator is adopted to ensure a zero static error of the capacitor energy. The approach achieves a good performance in the capacitor energy control.

With the development of optimal control theory, the time-domain optimal control approach is substantively investigated for inverter control [17]–[26]. Basically, different optimization problems with different optimized objectives, which are convergence rate [17], [18], H_∞ norm [19], [20], and LQ index [21]–[26], are constructed to design the controller gains.

In [17] and [18], the control law that includes state feedback gains and tracking gain (for the integrator) is designed by means of a linear matrix inequality (LMI) based optimization solution where a convergence rate is maximized. The minimum H_∞ norm optimization problem is employed in [19] to determine the control gains of the state feedback and integrator gains. But the integrator is for the root-mean-square tracking control. So far, in [17]–[19], the single controller is employed.

To further address the harmonic problem, multiple controllers are employed in [20]–[26]. In this condition, the selection of the high-dimension gains for the multiple controllers is generally not a simple task [25]. In [20], the gains are determined by means of the LMI solution of H_∞ optimization with regional poles placement (RPP). However, the H_∞ norm sometimes leads to an impractical control law because of the saturation of the control actuator [27]. In addition, the main shortcoming of the H_∞ control [19], [20] is the neglect of the physical constraint of the control input, so that it usually results in exorbitant gains that should be avoided.

An alternative solution is the linear quadratic regulation (LQR) [21]–[26]. The LQR supplies good control qualities, such as attractive gain and phase margins and robustness [28]. Hence, the LQR is adopted in [21]–[25]. However, the primary problem for the LQR method is the selection of the weight matrix $\boldsymbol{Q}$ for LQR, which tunes the performance of the system. Unfortunately, there is no direct relationship between the weight matrix and the system performance. Hence, the selection process is generally a subjective and annoying task. The trial-and-error method is used in [21] and [22]. To select the weight matrix better, Quan *et al.* [23] and Ufnalski *et al.* [25] have adopted the root locus and particle swarm optimization to optimally determine the entries of the weight matrix $\boldsymbol{Q}$. The root locus method in [23] is a pictorial method and lacks quantitative analysis. Hence, the resulted performance may not be exactly optimal. An extra user-defined performance index is used to select the best entries of $\boldsymbol{Q}$ in [25], which has achieved a satisfactory result. The performance is optimal from an application's point of view. Nevertheless, the user-defined performance index introduced in [25] is calculated by the errors and the differential value of the control input so that the offline determination procedure of the $\boldsymbol{Q}$ depends on the simulation model of the control system. The optimized procedure is continuously completed through a simulation period (the simulation time is 6 s in [25]). Another problem for LQR control is its high H_∞ index, because it has a different optimization direction compared to H_∞ control. The LQR endeavors to minimize the energy of the control input, whereas the H_∞ control maximize the disturbance-rejection ability leading to a big control input amount.

As in the classical multiple-loop control, the load current decoupling control can offer remarkable enhancement for the disturbance-rejection ability; however it is not used in [17]–[25]. This is probably because the internal model has been embedded as the tracking controller, then, it is considered that the disturbance is already rejected well. Actually, the disturbance-rejection ability depends on the high feedback gains of the controllers. Hence, in practice, one has to compromise between the disturbance-rejection ability and the harmonics or instability (may be led by the high gains). So far, few literatures have investigated the load current decoupling in such a state-space control structure [17]–[25]. In [26], a combined full-state and load current feedforward control is designed to reduce the number of needed oscillatory terms. The proposed feedforward control can compensate the load disturbance at steady state of output voltage, because it is assumed that the time derivative of the output voltage equals zero when calculating the feedforward gain matrices. To summarize, the features of many different controls are compared in Table I.

In this paper, first, a unified control structure for both α and β axes is adopted, then a load current decoupling control based on LQR is designed to remedy the deficiency of the LQR. A LQR with circle pole constraint in terms of LMI is first used to compute the state feedback control law. The approach can alleviate the parameter design burden for multiple controllers. Then, two general criteria are proposed to optimally utilize the load current. The LQ index and H_∞ norm are both optimized by the feedback and load current decoupling control, respectively, so that, first, the number of resonant controllers is decreased sharply; second, the fast dynamic response is achieved by relative smaller controller gains; third, the THD index of the output

TABLE I
SUMMARY OF DIFFERENT CONTROL STRATEGIES

	Transfer Function Model [3]–[8]	State-Space model			
		No IMP-based controller [9]–[14]	Including IMP-based controller (quantified optimal control)		
			Convergence rate [17], [18]	H_∞ control [19], [20]	LQR [21]–[26]
Advantages	Plenty of experienced methods and tools for designer; clear physical meaning for control design	Excellent dynamic performance can be achieved; no need for IMP-based controllers so that the implementation may be simple.	Control gains are derived by quantified calculation and do not need trial and error; some numerical indexes can be used to optimize control performance.		
			Fast transient response.	Optimized H_∞ norm leading to high disturbance-rejection ability	Attractive gain and phase margins and robustness; small feedback gains; smooth dynamic process.
Disadvantages	Control gains sometimes need trial and error; complicated to deal with MIMO and high-order systems	Some extra information (such as the time derivative of reference in [14]) may be needed to implement the control law; control laws need careful design to eliminate the static error; more mathematical knowledge are needed.	Lack clear physical meanings; compromise between different indexes; more mathematical knowledge are needed.		
			Actually, it is a particular case of the proposed LQR by setting weight matrix to zero and minimizing the radius of circle $D(q,\, r)$ (see Section III-A and Appendix A).	Ignore the physical constraint of the control input; exorbitant gains are usually resulted.	No explicit relationship between weight matrix and system performance; slow dynamic response if there are no other auxiliary optimal design, such as pole restriction or H_∞ norm optimization

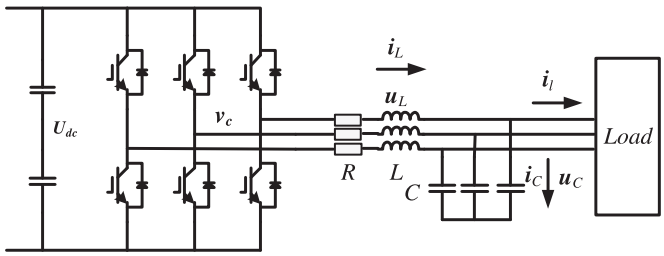

Fig. 1. Topology of the three-phase inverter with an *LC* filter.

voltage is reduced effectively when feeding linear loads or nonlinear loads, and the smaller voltage drop and faster recovering time under sudden load variation are accomplished. Those conclusions are proven by the simulation and experiment outcomes.

II. CONTROL STRUCTURE

A. Modeling of the Plant

As displayed in Fig. 1, the inverter adopts pulse width modulation (PWM) techniques to obtain a sinusoidal output voltage by the control input voltage $\boldsymbol{v}_c$. A state-space model can present the plant under the α–β reference frame [20], [23] as

$$\begin{cases} \dot{\boldsymbol{x}}_p = \boldsymbol{A}_p \boldsymbol{x}_p + \boldsymbol{B}_{p1} \boldsymbol{v}_c + \boldsymbol{B}_{p2} \boldsymbol{w}_p \\ \boldsymbol{y} = \boldsymbol{C}_p \boldsymbol{x}_p \end{cases} \tag{1}$$

where the state variable $\boldsymbol{x}_p = [\boldsymbol{i}_L\ \boldsymbol{u}_C]^T = [i_{L\alpha} + j i_{L\beta}\ u_{C\alpha} + j u_{C\beta}]^T$ denotes the inductor current and capacitor voltage, and $\boldsymbol{w}_p = \boldsymbol{i}_l = i_{l\alpha} + j i_{l\beta}$ represents the disturbance from the unknown load current, subscript "p" denotes plant. By applying a basic electric circuit theory for the *LC* filter, the matrices in (1) can be easily derived as

$$\boldsymbol{A}_p = \begin{bmatrix} -RL^{-1} & -L^{-1} \\ C^{-1} & 0 \end{bmatrix} \boldsymbol{B}_{p1} = \begin{bmatrix} L^{-1} \\ 0 \end{bmatrix} \boldsymbol{B}_{p2} = \begin{bmatrix} 0 \\ -C^{-1} \end{bmatrix}$$
$$\boldsymbol{C}_p = \begin{bmatrix} 0 & 1 \end{bmatrix} \tag{2}$$

where R, L, and C denote the resistor, inductance, and capacitance of the *LC* filter, respectively. To apply the discrete-time control technique, the state-space model is discretized with an extra state variable given by $\theta[k]$, which denotes the digital control delay

$$\begin{aligned} \boldsymbol{x}_p(k+1) &= \boldsymbol{A}_{dp} \boldsymbol{x}_p(k) + \boldsymbol{B}_{dp1} \boldsymbol{\theta}(k) + \boldsymbol{B}_{dp2} \boldsymbol{w}_p(k) \\ \boldsymbol{\theta}(k+1) &= \boldsymbol{v}_c(k). \end{aligned} \tag{3}$$

The discrete-time system matrices are derived using the zero-hold method as

$$\begin{aligned} \boldsymbol{A}_{dp} = e^{\boldsymbol{A}_p T_s}, \boldsymbol{B}_{dp1} &= \int_0^{T_s} e^{\boldsymbol{A}_p t} dt \boldsymbol{B}_{p1}, \boldsymbol{B}_{dp2} \\ &= \int_0^{T_s} e^{\boldsymbol{A}_p t} dt \boldsymbol{B}_{p2} \end{aligned} \tag{4}$$

where T_s represents the sampling period. The discretization computation could be done by function c2d() supplied by MATLAB.

In this model, the assumptions are considered to construct the following optimal voltage controller: 1) The disturbance (load current) is a finite energy signal and varies slowly during the sampling period [12]. This assumption is always satisfied, because in a real-word application the infinite energy signal does not exist, and the sampling period is always short compared

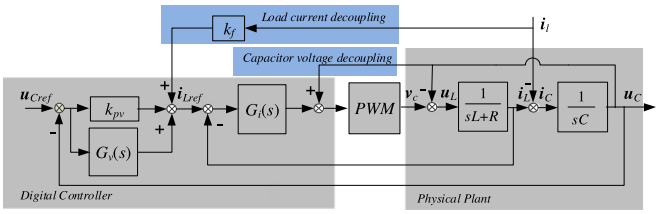

Fig. 2. Classical dual-loop control for the inverter.

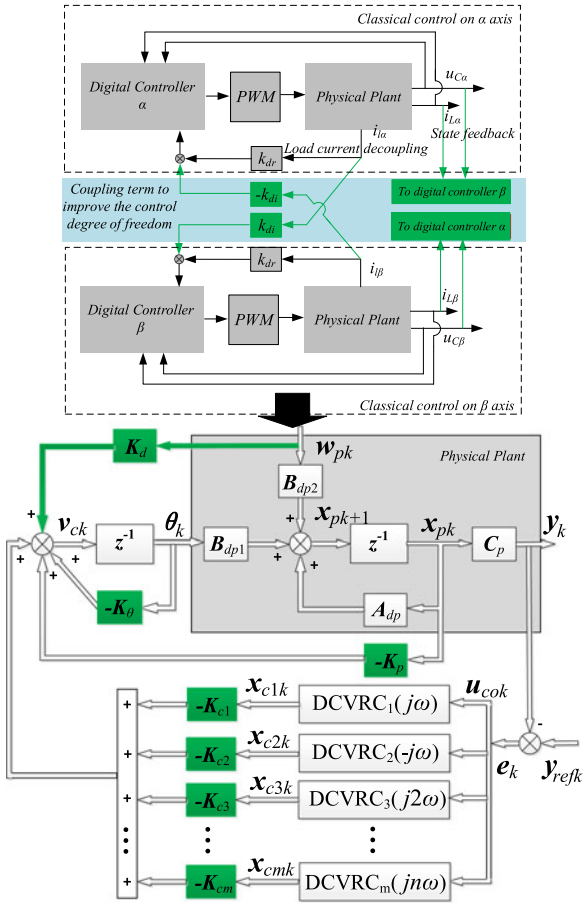

Fig. 3. Evolution of the proposed control approach.

to the fundamental period. Otherwise any real system will be instable under the disturbing of the infinite energy signal. 2) The dc-link voltage is well controlled as an ideal dc source by other dc power supplies, such as the battery. This assumption can also be satisfied by the appropriate control design for the dc voltage. If the dc voltage is not controlled well, it may cause high THD, stability issue, and inverting failure. Fortunately, the dc bus voltage can be used to decouple the negative influence.

B. Control of the Voltage

Fig. 2 shows the classical dual-loop control structure, whereas Fig. 3 shows how the proposed control approach is derived. From Fig. 3, the multiple discrete-time complex variable resonant controllers (DCVRCs) are included in the model to generalize the proposed method. The variable $n = \pm 1, \pm 2 \ldots$ denotes the order of the DCVRCs, and m represents the number of the DCVRCs. The number of resonant terms (DCVRCs) depends on the system topology, because different topologies and coordinate systems have different harmonic distributions [24]. Detailed discussion for this topic has been presented in [24]. However, for the α/β frame control of three-phase three-wire system, the number of the DCVRCs is reduced effectively by the proposed control.

The DCVRC is expressed as follows:

$$\boldsymbol{x}_c(k+1) = e^{j\omega T_s}\boldsymbol{x}_c(k) + T_s\boldsymbol{u}_{co}(k) \tag{5}$$

where $\boldsymbol{x}_c = x_{c\alpha} + jx_{c\beta}$ and $\boldsymbol{u}_{co} = u_{co\alpha} + ju_{co\beta}$ indicate the auxiliary state variable and the input variable of the controller, respectively. According to the method of transfer function computation from the state-space model, it has

$$\frac{\boldsymbol{x}_c}{\boldsymbol{u}_{co}} = (z - e^{j\omega T_s})^{-1}T_s = \frac{T_s}{z - e^{j\omega T_s}} \tag{6}$$

from which we can see that the DCVRC provides infinite gain only to a positive sequence input complex variable of frequency ω and attenuates the negative sequence complex variable. In contrast to the scalar resonant controller (SRC), the DCVRC requires fewer states in its implementation and provides discrimination between positive and negative sequence components. This identification of positive and negative sequence signals has been successfully applied to current control for three-phase inverters [29]. Another advantage of the complex variable control under the α–β reference frame is to supply one more control degree of freedom, as shown in Fig. 3.

As shown in Fig. 3, DCVRCs and the model of the plant are integrated by the following equation:

$$\boldsymbol{u}_{co} = \boldsymbol{e} = \boldsymbol{y}_{\text{ref}} - \boldsymbol{C}_p\boldsymbol{x}_p. \tag{7}$$

Substituting (7) into (3), then combining (3), the augmented state-space model of the control system can be derived as

$$\begin{cases} \boldsymbol{x}(k+1) = \boldsymbol{A}\boldsymbol{x}(k) + \boldsymbol{B}_1\boldsymbol{v}_c(k) + \boldsymbol{B}_2\boldsymbol{w}_p(k) + \boldsymbol{R}_r\boldsymbol{y}_{\text{ref}}(k) \\ \boldsymbol{y} = \boldsymbol{C}\boldsymbol{x} \end{cases} \tag{8}$$

where $\boldsymbol{x} = [\boldsymbol{x}_p\, \theta\, \boldsymbol{x}_{c1}\, \boldsymbol{x}_{c2}\, \cdots\, \boldsymbol{x}_{cm}]^T$ represents the augmented state variables and $\boldsymbol{y}_{\text{ref}}$ denotes output voltage reference. The corresponding matrices are given as

$$\boldsymbol{A} = \begin{bmatrix} \boldsymbol{A}_{dp} & \boldsymbol{B}_{dp1} & 0 & 0 & 0 & 0 & 0 \\ 0 & 0 & 0 & 0 & 0 & 0 & 0 \\ -T_s\boldsymbol{C}_p & 0 & e^{j\omega T_s} & & & & \\ -T_s\boldsymbol{C}_p & 0 & & e^{-j\omega T_s} & & & \\ -T_s\boldsymbol{C}_p & 0 & & & \ddots & & \\ -T_s\boldsymbol{C}_p & 0 & & & & e^{jn\omega T_s} & \\ -T_s\boldsymbol{C}_p & 0 & & & & & e^{-jn\omega T_s} \end{bmatrix} \tag{9}$$

$$\boldsymbol{B}_1 = \begin{bmatrix} 0 & 1 & 0 & \cdots & 0 & 0 \end{bmatrix}^T \tag{10}$$

$$\boldsymbol{C} = \begin{bmatrix} \boldsymbol{C}_p & 0 & 0 & \cdots & 0 & 0 \end{bmatrix} \tag{11}$$

$$\boldsymbol{B}_2 = \begin{bmatrix} \boldsymbol{B}_{dp2} & 0 & 0 & \cdots & 0 & 0 \end{bmatrix}^T \tag{12}$$

$$\boldsymbol{R}_r = \begin{bmatrix} 0 & 0 & 1 & \cdots & 1 & 1 \end{bmatrix}^T. \tag{13}$$

The dimension of those matrices is related to the number of the DCVRCs: $d = m + 3$ where d denotes the dimensions. From Fig. 3, the control input consists of state feedback $\boldsymbol{K}x$ and decoupling term $\boldsymbol{K}_d\boldsymbol{w}_p$. For m DCVRCs, there $m + 3$ undetermined complex coefficients are included by the augmented state feedback control law. The control input is expressed as

$$\begin{aligned} \boldsymbol{v}_c = & -\boldsymbol{K}\boldsymbol{x} + \boldsymbol{K}_d\boldsymbol{w}_p = -\left[\boldsymbol{K}_{p1}^{(i)}\ \boldsymbol{K}_{p2}^{(\mathbf{u})}\ \boldsymbol{K}_\theta \boldsymbol{K}_{c1}^{(+1)}\right. \\ & \left. \boldsymbol{K}_{c2}^{(-1)}\ \boldsymbol{K}_{c3}^{(+2)}\ \boldsymbol{K}_{c4}^{(-2)} \cdots \boldsymbol{K}_{cm}^{(+n)}\right]\boldsymbol{x} + \boldsymbol{K}_d\boldsymbol{w}_p. \end{aligned} \tag{14}$$

Comparing Fig. 2 with Fig. 3, the improvements of the proposed control are demonstrated as follows.

1) The parameter design of the dual-loop control is usually based on classical methods, such as Bode plot or root locus. The inner current loop must be designed first, then the outer voltage loop can be determined. This design method is complicated, and the designed parameters may require further trial and error in practice. Furthermore, this method is not easy to deal with the multiple controllers and complex variable controllers. The proposed control approach offers a simple design process (even with multiple and complex parameters) without trial and error for the parameters. Because all of the feedback gains are translated into the state feedback control law, they can be determined by a quantified optimal method.
2) The classical method is hard to process complex variable control parameters, therefore, the SRC is always adopted in the dual-loop control. In SRC application, a phase compensation is necessary [6]. While in the proposed control method, voltages on the α- and β-axis are controlled simultaneously as a complex variable. The coupled gains between α and β axes (as the imaginary parts of the complex gains) is adopted to increase the control degree of freedom, as shown in Fig. 3, thereby the phase compensation can be omitted.
3) As revealed in Fig. 2, the load current decoupling is designed to decouple the disturbance thanks to the direct physical meanings; however, it is because of the explicit physical meaning that k_f is always set to one. Moreover, this decoupling term is imposed on the reference of the current, consequently, the decoupling performance is deteriorated by the inner current loop. While in the proposed control method, the load current is directly imposed on the control input to decoupling the disturbance, and the gain is expanded to an adjustable complex value $\boldsymbol{K}_d = k_{dr} + jk_{di}$. This supplies two degrees of freedom to improve the control performance. The design of $\boldsymbol{K}_d$ has no explicit physical meanings but can be selected based on other criteria, which will be discussed later.

III. Control Algorithm

In this paper, the LMI approach will be adopted to compute the control parameters. The LMI-based optimization problem can be solved by the MATLAB toolbox conveniently. However, the LMI toolbox in MATLAB can only deal with the real number LMI. Therefore, let us first illustrate the isomorphic relationship between a complex variable and real matrix given by

$$a + jb \triangleq \begin{bmatrix} a & -b \\ b & a \end{bmatrix}. \tag{15}$$

Based on (15), a complex matrix can be equivalently expressed by a dimension-added real matrix, after which, the corresponding complex variables become dimension-added real vectors. For example, under this map, the state-space model of DCVRC becomes

$$\begin{aligned} \begin{bmatrix} x_{c\alpha}(k+1) \\ x_{c\beta}(k+1) \end{bmatrix} = & \begin{bmatrix} \cos(\omega T_s) & -\sin(\omega T_s) \\ \sin(\omega T_s) & \cos(\omega T_s) \end{bmatrix} \begin{bmatrix} x_{c\alpha}(k) \\ x_{c\beta}(k) \end{bmatrix} \\ & + T_s \begin{bmatrix} u_{co\alpha}(k) \\ u_{co\beta}(k) \end{bmatrix}. \end{aligned} \tag{16}$$

It is supposed hereafter that the symbols of those complex variables in (8) represent the equivalent dimension-added real matrices and the dimension-added real vectors without influencing the correctness of the statement.

The design of the proposed controller can be divided into state feedback and disturbance decoupling. In previously reviewed literatures [17]–[25], the load current decoupling is not adopted, therefore, the fast dynamic response and disturbance-rejection ability must be achieved by the state feedback. However, in the proposed method, the fast dynamic response and disturbance-rejection ability can be achieved by the disturbance decoupling control, therefore the feedback control can pay more attention on other optimization indices, such as the L_2 norm of the state variable.

In what follows, first, an improved discrete-time LQR is adopted to design the state feedback to minimize the weighting time-domain L_2 norm. The minimization of L_2 norm will result in satisfactory gain and phase margins, small state feedback gains and robustness. Second, two general criteria for the load current decoupling are introduced to improve the dynamic performance.

A. State Feedback Control Law

With the proposed control law (14), the closed-loop system is expressed as follows:

$$\begin{aligned} \boldsymbol{x}(k+1) = & (\boldsymbol{A} - \boldsymbol{B}_1\boldsymbol{K})\boldsymbol{x}(k) + (\boldsymbol{B}_2 + \boldsymbol{B}_1\boldsymbol{K}_d)\boldsymbol{w}_p(k) \\ & + \boldsymbol{R}_r\boldsymbol{y}_{\text{ref}}(k). \end{aligned} \tag{17}$$

To design the optimal state feedback law $\boldsymbol{K}$, the LQ performance index that includes the weighting L_2 norm of $\boldsymbol{x}$ is defined as

$$J = \sum_{k=0}^{\infty} \left(\boldsymbol{x}^T(k)\boldsymbol{Q}\boldsymbol{x}(k) + \boldsymbol{u}^T(k)\boldsymbol{R}\boldsymbol{u}(k)\right) \tag{18}$$

where $\boldsymbol{Q} \geq 0$, $\boldsymbol{R} > 0$. For the open-loop system (8) and given $\boldsymbol{Q}_0$ and $\boldsymbol{R}$, if there exist a symmetric positive definite matrix $\boldsymbol{W}$, positive matrices $\boldsymbol{M}$ and $\boldsymbol{Q}_{\text{inv}}$, and matrix $\boldsymbol{V}$, then the optimization problem

$$\min_{\mathbf{W}_1,\ \mathbf{V}_1,\ \mathbf{M},\ \mathbf{Q}_{\text{inv}}} \quad \text{Trace}(\boldsymbol{M}) \tag{19}$$

$$\text{s.t.} \begin{bmatrix} -r^2\boldsymbol{W} & (\boldsymbol{AW} - \boldsymbol{B}_1\boldsymbol{V} - q\boldsymbol{W})^{\mathrm{T}} & \boldsymbol{W} & \boldsymbol{V}^{\mathrm{T}} \\ (\boldsymbol{AW} - \boldsymbol{B}_1\boldsymbol{V} - q\boldsymbol{W}) & -\boldsymbol{W} & & \\ \boldsymbol{W} & & -\boldsymbol{Q}_{\text{inv}} & \\ \boldsymbol{V} & & & -\boldsymbol{R}^{-1} \end{bmatrix} < 0 \tag{20}$$

$$\begin{bmatrix} \boldsymbol{M} & \boldsymbol{I} \\ \boldsymbol{I} & \boldsymbol{W} \end{bmatrix} > 0 \tag{21}$$

$$\boldsymbol{Q}_{\text{inv}} < \boldsymbol{Q}_0^{-1} \tag{22}$$

is feasible with the solution $\hat{\boldsymbol{W}}, \hat{\boldsymbol{V}}, \hat{\boldsymbol{M}}, \hat{\boldsymbol{Q}}_{\text{inv}}$, resulting in $\boldsymbol{v}_c = -\boldsymbol{K}\boldsymbol{x} = -\hat{\boldsymbol{V}}\hat{\boldsymbol{W}}^{-1}\boldsymbol{x}$ as the minimum LQ index control that ensures 1) the closed-loop poles are locating in the circle $D(q, r)$ whose radius is r and center is q; and 2) the LQ index $J \leq J^* = \boldsymbol{x}_0^T \hat{\boldsymbol{W}}^{-1}\boldsymbol{x}_0 = \text{Trace}(\boldsymbol{W}^{-1})$ is true where $\boldsymbol{x}_0$ denotes the initial value of $\boldsymbol{x}$, and Trace() means trace of a matrix. The proof of these can be found in [30] and [31]. For the readability, the proof is summarized in Appendix. Here, the following two remarks are given.

Remark 1: To avoid selecting the weight matrix $\boldsymbol{Q}$, the user-defined $\boldsymbol{Q}$ is modified to an optimization variable $\boldsymbol{Q}^{-1} = Q_{\text{inv}}$ to extend the feasible region. This modification removes the subjective $\boldsymbol{Q}$ selection task and meanwhile enlarges the feasible region. The user-defined matrix $\boldsymbol{R}$ is reserved in (20) because there is no loss of generality in taking $\boldsymbol{R} = \boldsymbol{I}$ where $\boldsymbol{I}$ denotes identity matrix [28]. Additionally, lower bound $\boldsymbol{Q}_0$ is also set to avoid the resulted weights becoming too low. In general, the high state weighting is needed to provide a technique to place closed-loop poles [28]. Hence, the modification gives abundant degrees of freedom to place the closed-loop poles as well.

Remark 2: Through setting $D(q, r)$ in unit circle, the closed-loop stability is guaranteed easily.

B. H_∞ Norm Criterion for Decoupling

For the general purpose of utilizing the load current to reject the disturbance, a H_∞ norm criterion is proposed. As it is well known that the H_∞ norm exactly reflects the disturbance-rejection ability. Applying the discrete-time bounded real lemma [32] to system (17), it has the following inequality:

$$\begin{bmatrix} \boldsymbol{A} - \boldsymbol{B}_1\boldsymbol{K} & \boldsymbol{B}_2 + \boldsymbol{B}_1\boldsymbol{K}_d \\ \boldsymbol{C} & \end{bmatrix}^T \begin{bmatrix} \boldsymbol{P} & \\ & \boldsymbol{I} \end{bmatrix} \begin{bmatrix} \boldsymbol{A} - \boldsymbol{B}_1\boldsymbol{K} & \boldsymbol{B}_2 + \boldsymbol{B}_1\boldsymbol{K}_d \\ \boldsymbol{C} & \end{bmatrix} - \begin{bmatrix} \boldsymbol{P} & \\ & \gamma^2\boldsymbol{I} \end{bmatrix} < 0 \tag{23}$$

where $\boldsymbol{P}$ represents the symmetric positive definite Lyapunov matrix. If (23) holds, then the frequency-domain H_∞ norm satisfies

$$\|T_{\mathbf{wy}}(z)\|_\infty = \sup_{\|\mathbf{w}_p\| \neq 0} \frac{\|\boldsymbol{y}\|_2}{\|\boldsymbol{w}_p\|_2} \leq \gamma \tag{24}$$

where $\|\cdot\|_2$ represents the time-domain L_2 norm, $\|\cdot\|_\infty$ denotes the frequency-domain H_∞ norm, and "sup" means supremum. Observing (23), with the determined $\boldsymbol{K}$, (23) can be used to design an optimal decoupling coefficient that minimizes the H_∞ norm. From (23), the following optimization framework can be derived to compute the minimum H_∞ norm decoupling gains [detailed derivation illustrated in Appendix B; also see (26) shown at the bottom of this page]:

$$\min_{\rho,\ \boldsymbol{W},\ \boldsymbol{K}_d} \quad \rho \tag{25}$$

If the optimization problem is feasible with the solution $\hat{\rho}$,$\hat{\boldsymbol{W}}$,$\hat{\boldsymbol{K}}_d$, then $\hat{\boldsymbol{K}}_d$ is the optimal H_∞ disturbance decoupling control law under the determined state feedback control law. The optimal decoupling will ensure the H_∞ norm supremum: $\|T_{\mathbf{wy}}(s)\|_\infty \leq \gamma^* = \sqrt{\hat{\rho}}$. According to the physical significance of the H_∞ norm, the disturbance-rejection ability will be improved.

C. Zero-Dynamic Criterion for Decoupling

In Section III-B, the optimization frame can yield the optimal H_∞ disturbance decoupling control law. In this section, how the optimal H_∞ disturbance decoupling term influences the distribution of the closed-loop zeros and poles for the disturbance-output transfer function (output impedance) is initially studied. The transfer function is computed by the following:

$$T_{wy}(z) = \frac{\boldsymbol{y}}{\boldsymbol{w}_p} = \boldsymbol{C}(z\boldsymbol{I} - \boldsymbol{A} + \boldsymbol{B}_1\boldsymbol{K})^{-1}(\boldsymbol{B}_2 + \boldsymbol{B}_1\boldsymbol{K}_d). \tag{27}$$

Variable z is the z-transformation operator.

Fig. 4 shows the distribution changes of the closed-loop zeros with the different disturbance decoupling strategies. The poles are located by optimal LQ state feedback $\boldsymbol{K}$, which is designed from the optimization frame (19)–(22) with the circle D(0.5, 0.495). Only one DCVRC is adopted to acquire a concise diagram that will not influence the correctness of the analysis.

$$\text{s.t.} \begin{bmatrix} -\boldsymbol{W} & & (\boldsymbol{A} - \boldsymbol{B}_1\boldsymbol{K}\boldsymbol{W})^T & (\boldsymbol{C}\boldsymbol{W})^T \\ & -\rho\boldsymbol{I} & (\boldsymbol{B}_2 + \boldsymbol{B}_1\boldsymbol{K}_d)^T & \\ (\boldsymbol{A} - \boldsymbol{B}_1\boldsymbol{K}\boldsymbol{W}) & \boldsymbol{B}_2 + \boldsymbol{B}_1\boldsymbol{K}_d & -\boldsymbol{W} & \\ \boldsymbol{C}\boldsymbol{W} & & & -\boldsymbol{I} \end{bmatrix} < 0 \tag{26}$$

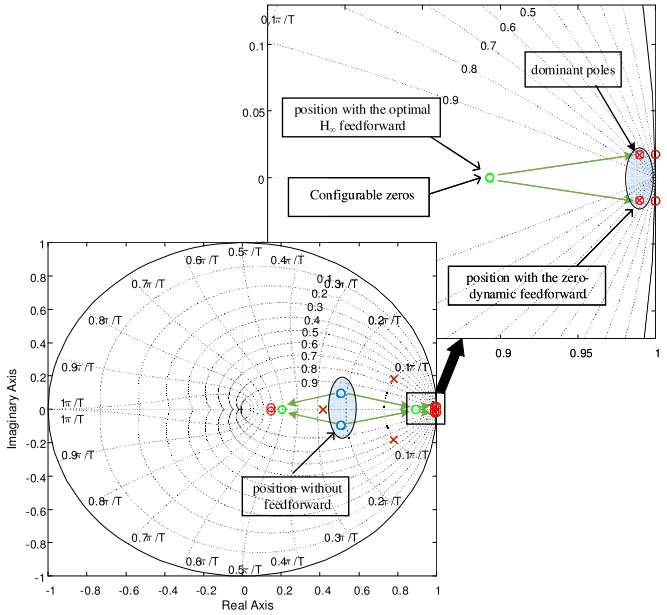

Fig. 4. Distribution changes of the closed-loop zeros and poles with the different decoupling strategies.

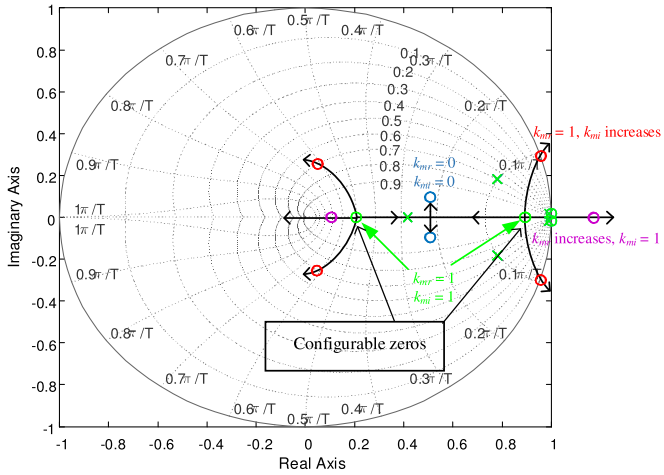

Fig. 5. Configurable zeros move with k_{mr} and k_{mi} varying.

TABLE II
PARAMETERS OF THE THREE-PHASE INVERTER

Variable	Significance	Value
L	Inductance	2 mH (1.85–2.15 mH for experiment)
C	Capacitance	30 μF
R	Inductor resistance	0.05 Ω
f_s	Switch and Sampling frequency	18000 Hz
	Output voltage peak	311 V
	DC-link voltage	630 V

According to (27) and Fig. 4, the optimal decoupling just modifies two pairs of zeros, called *configurable zeros* here. It can be revealed that the *configurable zeros* are forced onto the real axis by the optimal H_∞ decoupling. Other zeros and poles are not affected.

Actually, if rewriting $\boldsymbol{K}_d$ as $\boldsymbol{K}_d = k_{dr} + jk_{di}$, it can be find that the *configurable zeros* will move with k_{dr} and k_{di} varying, respectively. This enlightens us to collocate the *configurable zeros* close to the dominant poles that are introduced by the DCVRC. Then, the dynamic caused by the sudden load variation will be weakened or even eliminated. Hence, it is named here as zero-dynamic decoupling. With the initial position determined by optimal H_∞ norm criterion, two modulation parameters are defined as $\boldsymbol{K}_d = k_{mr}k_{dor} + jk_{mi}k_{doi}$ where $\boldsymbol{K}_{do} = k_{dor} + jk_{doi}$ is the optimal H_∞ decoupling control law calculated by (25). The varying trajectory of the *configurable zeros* with k_{mr} and k_{mi} changing is shown in Fig. 5. From the beginning of the optimal H_∞ decoupling ($k_{mr} = 1\, k_{mi} = 1$), when (k_{mr}, k_{mi}) reduces to (0, 0), the zeros will move back to the position without decoupling. While remaining $k_{mi} = 1$ and increasing k_{mr}, the zeros will shift along with the real axis. When k_{mi} increases with $k_{mr} = 1$, the zeros will deviate the real axis. Hence with the reference position of the optimal H_∞ decoupling, it is convenient to relocate the zeros nearby the dominant poles by tuning k_{mr} and k_{mi}. As shown the right side in Fig. 4, the dominant poles are overlapped by the configurable zeros. In the tuning process, the zero position of optimal H_∞ decoupling serves as a reference. Because, the large increment of H_∞ norm is not expected while the zeros deviate the optimal H_∞ location. Fortunately, in this paper, the zero-dynamic decoupling do not reduce the H_∞ norm remarkably.

It is worth noting that the accurate value of $\boldsymbol{K}_d$ to offset the dominant poles can be computed theoretically. However, in this paper, it is complicated, because a least four-order matrix variable needs to perform matrix inversion, as described in (27). Moreover, with the help of the modulation parameters k_{mr} and k_{mi} and initial location of optimal H_∞ decoupling, it is easy to find the zero-dynamic decoupling coefficient. Finally, the design procedure of the proposed control strategy can be summarized as follows:

Step 1) build augmented system model (8);
Step 2) calculate the state feedback control law by (19)–(22);
Step 3) compute the optimal H_∞ decoupling law by (25) and (26);
Step 4) tune the modulation parameters k_{mr} and k_{mi} with the initial location of optimal H_∞ decoupling derived from Step 3).

IV. Case Study and Performance Analysis

A. Performance Comparison

To highlight the improved performance of the proposed method, the classical dual-loop control and optimal H_∞ control proposed in [20] are compared via the Bode plot analysis. Table II lists all system parameters used in this study. For the proposed approach, the circle is chosen as $D(0.5, 0.495)$ and the lower bound $\boldsymbol{Q}_0$ is set to diag([1 10 1 1]) which results in a H_∞ norm of 9.78. The parameter setting of $D(q, r)$ and $\boldsymbol{Q}_0$ is cursory. Because, it will be proven that even an unsatisfactory state feedback law can also be improved by the

TABLE III
PARAMETER COMPARISON OF DIFFERENT APPROACHES

	Optimal H_∞ Control With RPP [20]	LQR Without Decoupling	Optimal H_∞ Norm Decoupling	Zero-Dynamic Decoupling	Dual-Loop Control
ρ		95.694	47.041	57.779	
γ	8.8	9.78	6.86	7.6	24.2
Control law	$[19.134 + j0.023,$ $1.30 + j0.0097,$ $-660.785 - j65.47].$	$[8.995 + j0.01456,$ $0.0156 + j0.00487,$ $-0.0162 + j0.00036,$ $-170.87 - j25.805].$	$5.9756 + j0.00867$	$8.695 + j0.5374$	$k_{pi} = 8,$ $k_{pv} = 0.03,$ $k_{rv} = 40$

proposed decoupling control algorithm. Then, based on the yielded state feedback, the optimal H_∞ decoupling law is computed as $\boldsymbol{K}_d = [5.9756 + j0.00867]$, which leads to a H_∞ norm upper bound of 6.86, and the zero-dynamic decoupling law is tuned to eliminate the dominant dynamic. The optimal H_∞ control with RPP is designed with $\sigma = 250$, $r = 6000$, and $\theta = \pi / 2$ according to the guideline in [20]. Equation (27) also can be used to compute the output impedance (disturbance-output transfer function) in [20]. For the classical dual-loop control, the impedance can be computed as

$$T_{\text{dis\_dl}} = \frac{u_c}{i_l} = \frac{(k_f k_{pi} - sL - R - k_{pi})(s^2 + \omega^2)}{sC(sL + R + k_{pi})(s^2 + \omega^2) + (k_{pv}s^2 + k_{rv}s + k_{pv}\omega^2)k_{pi}}. \tag{28}$$

The parameters are selected as: $k_{pi} = 8$ led into 1800 Hz bandwidth, $k_{pv} = 0.03$ led into 200 Hz bandwidth, and $k_{rv} = 40$ referred to [6]. The selected bandwidths will lead to a fast dynamic response based on the classical control theory. The summarized control laws are listed in Table III.

First, the LQR can minimize the time-domain L_2 norm, whose physical meaning is the energy of the state variable and input, which will result in a smooth dynamic response and a small control gains. The control law shown in Table III can prove this point.

Second, in this paper, the supremum of the H_∞ norm γ, whose physical meaning is the maximum value of the output impedance, is adopted to design the load current decoupling control. It is a quantized index to directly evaluate the disturbance-rejection ability. The minimization of γ can reduce the maximum value of the output impedance (as shown in Fig. 6, the proposed H_∞ decoupling control has the minimum–maximum value of the impedance), thereby improving the disturbance-rejection ability.

Third, the zero-dynamic criterion for the load current decoupling has two physical meanings: 1) the value of the output impedance can be reduced within a range of low frequencies (as shown in Fig. 6, the impedance of zero-dynamic decoupling control is smallest within 10–1000 Hz) thereby decreasing the THD of the output voltage when feeding a nonlinear load (this is also why the proposed control can achieve lower THD with reduced controllers); 2) the slow dynamic mode can be eliminated by the decoupling term, thereby improving the dynamic response (this is why the parameters of the controller do not need high gains).

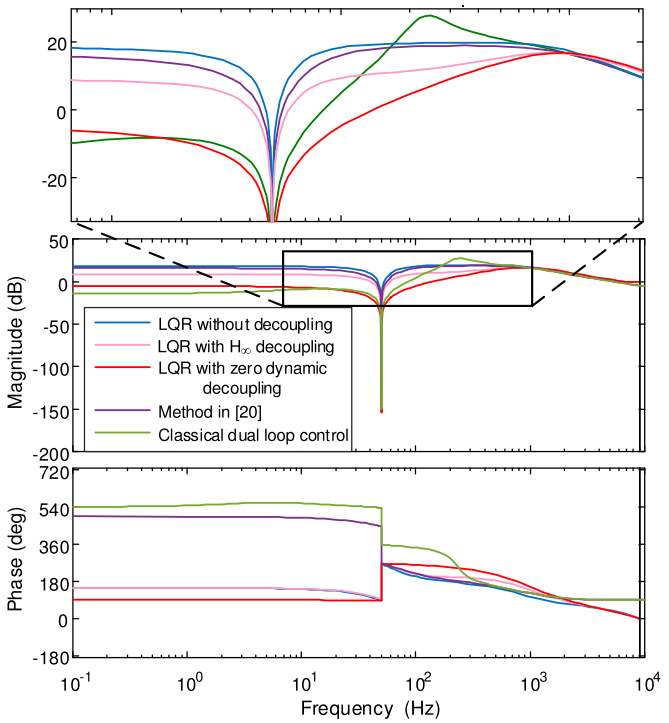

Fig. 6. Comparative Bode diagrams of the proposed LQR without load current decoupling, with the optimal H_∞ load current decoupling, with the zero-dynamic load current decoupling, the optimal H_∞ control proposed in [20], and the classical dual-loop control with load current decoupling.

In addition, from Fig. 6, the classical dual-loop control with load current decoupling has the biggest γ. This is because the classical design of the dual-loop control does not consider the H_∞ norm. Although it is possible to design a small γ through the selection of the control parameters (not the decoupling gain), it is a blind process to design these parameters, because there is no direct design criterion for this target.

The summarized H_∞ norm upper bounds and control laws are listed in Table III for a clear comparison. Note from Table III that the optimal H_∞ control with RPP [20] has a larger H_∞ norm upper bound. This is because in [20], the H_∞ LMI and D-stability constraints share the same Lyapunov matrix. This processing method introduces certain conservative property.

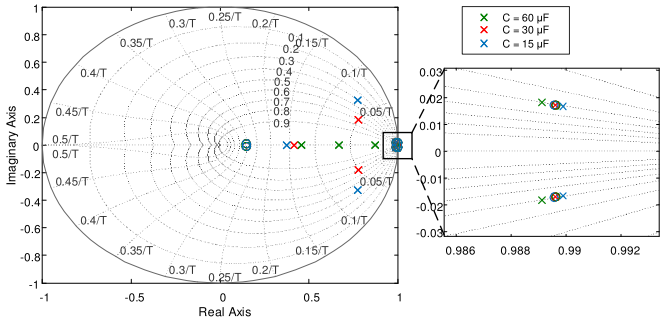

Fig. 7. Zero-pole distribution with capacitance varying.

B. Robust Analysis

To demonstrate the robustness of the proposed algorithm, the zero-pole distribution with capacitance varying is shown in Fig. 7. It can be concluded from Fig. 7 that the capacitance has little influence on the distribution of the dominant poles and the configurable zeros. Hence, the dominant dynamic elimination property has a strong robustness to capacitance variation. The similar conclusion can also be drawn with the variation of inductance, but it is not presented here due to the limited space. Furthermore, the control performance under low frequency usually depends on the distribution of the dominant poles, therefore, the proposed algorithm will exhibit a robust performance under parameter variation.

V. Simulation Verification

The proposed control algorithm is simulated in MATLAB/Simulink. In the simulation, only one DCVRC in fundamental positive sequence is adopted. The classical dual-loop control and the optimal H_∞ control proposed in [20] are compared. The adopted parameters are listed in Table III.

A linear load shown in Fig. 9(a), where 29 Ω results in 5 kW power, is adopted to verify the dynamic performance of the proposed control algorithm. The simulation results of the five control approaches are shown in Fig. 8, where $\boldsymbol{e} = e_\alpha + je_\beta$ denotes the voltage error. The load is connected and disconnected suddenly to the inverter to test the dynamic performance of the voltage control. As displayed in Fig. 8(a), the optimal H_∞ control with RPP performs the fast recovering time of 15 ms, however, it is resulted from the large control gains. It is feasible in the simulation case, but in practice, it may lead into instability. Moreover, the 69 V voltage drop (amplitude of $\boldsymbol{e}$ computed by $\sqrt{e_\alpha^2 + e_\beta^2}$) is not the smallest even in such high gains. Comparatively, the dynamic response of the LQR shown in Fig. 8(b) exhibits a poor performance with approximate 22 ms recovering time and 83 V voltage drop. As shown in Fig. 8(c), with the backing of the optimal H_∞ decoupling, the recovering time is shortened to 16 ms, and the voltage drop is reduced to 53 V.

In addition, the best performance is achieved by the zero-dynamic load current decoupling. The corresponding result is shown in Fig. 8(d), which manifests that the voltage almost experiences the zero-dynamic process under the abrupt load; and the voltage drop is 51 V, which is even less than the optimal H_∞ decoupling control. Fig. 8(e) shows the simulation result of the classical dual-loop control with load current decoupling. The recovering time is about 10 ms, and the voltage drop is 71 V. Moreover, to evaluate the system behavior under an unbalanced load condition, the loads of phases B and C are connected first at 0.1 s, and the load of phase A is connected to the inverter at 0.2 s. Accordingly, the DCVRC$(-j\omega)$ is embedded in the control system. As shown in Fig. 8(f), the proposed control strategy performs well under the unbalanced load condition.

VI. Experiment Verification

The proposed control algorithm has also been verified by experiments with a prototype 5-kVA *LC*-inverter bench. The inductor currents and capacitor voltages are measured to implement the state feedback control. The load currents are also needed to realize the decoupling control. However, an observer can be employed to avoid the extra sensor [12]. In this paper, the same linear observer as in [12] is used. Furthermore, the sinusoidal PWM technique is used to generate the control inputs $\boldsymbol{v}_c$. Table II lists all system parameters used in this study. The inductance is variable in practical experiment because the magnetic core of the inductor is a Fe–Si–Al magnet ring. Then, the inductance will shift with the current due to the saturation of the magnetic core. However, for the parameter design, the nominal inductance parameter is chosen as 2 mH. A 32-b floating-point TMS320LF28335 DSP is used to realize the control algorithm in the experiment.

A. Dynamic Performance Comparison

Similar to the simulation, the abrupt linear load shown in Fig. 9(a) is adopted to test the dynamic performance of the proposed control algorithm. The DCVRC configuration and gain coefficients are also the same as the simulation, as shown in Table III. Five comparative experiments are conducted, as shown in Fig. 10.

Fig. 10(a) manifests that the optimal H_∞ control proposed in [20] is unstable. The control gains are too high to realize in practice. In [20], the control algorithm is feasible because of the bigger capacitance. This is due to the natural properties of the optimal H_∞ control, which maximizes the disturbance-rejection ability without any consideration of the physical limitation of the control input. The ability of disturbance-rejection is positively related to the capacitance of the *LC* filter. In the case of this test, the disturbance-rejection ability designed by the method mentioned in [20] cannot be realized by the 30 μF capacitance so that it appears to be an instability phenomenon. However, the capacitance of the capacitor adopted in [20] is 300 μF, which is ten times that of its counterpart in this research. This is why the design approach works well in [20] but fails in this paper.

Fig. 10(b) shows the result of the classical dual-loop control with load current decoupling, the recovering time is about 18 ms, and the voltage drop is 89 V. Moreover, as shown in Fig. 10(c), the LQR without load current decoupling experiences an 83.7 V voltage drop when the load suddenly connects to the inverter and the recovering time is about 20 ms. By comparison, the voltage drop and recovering time of optimal H_∞ load current

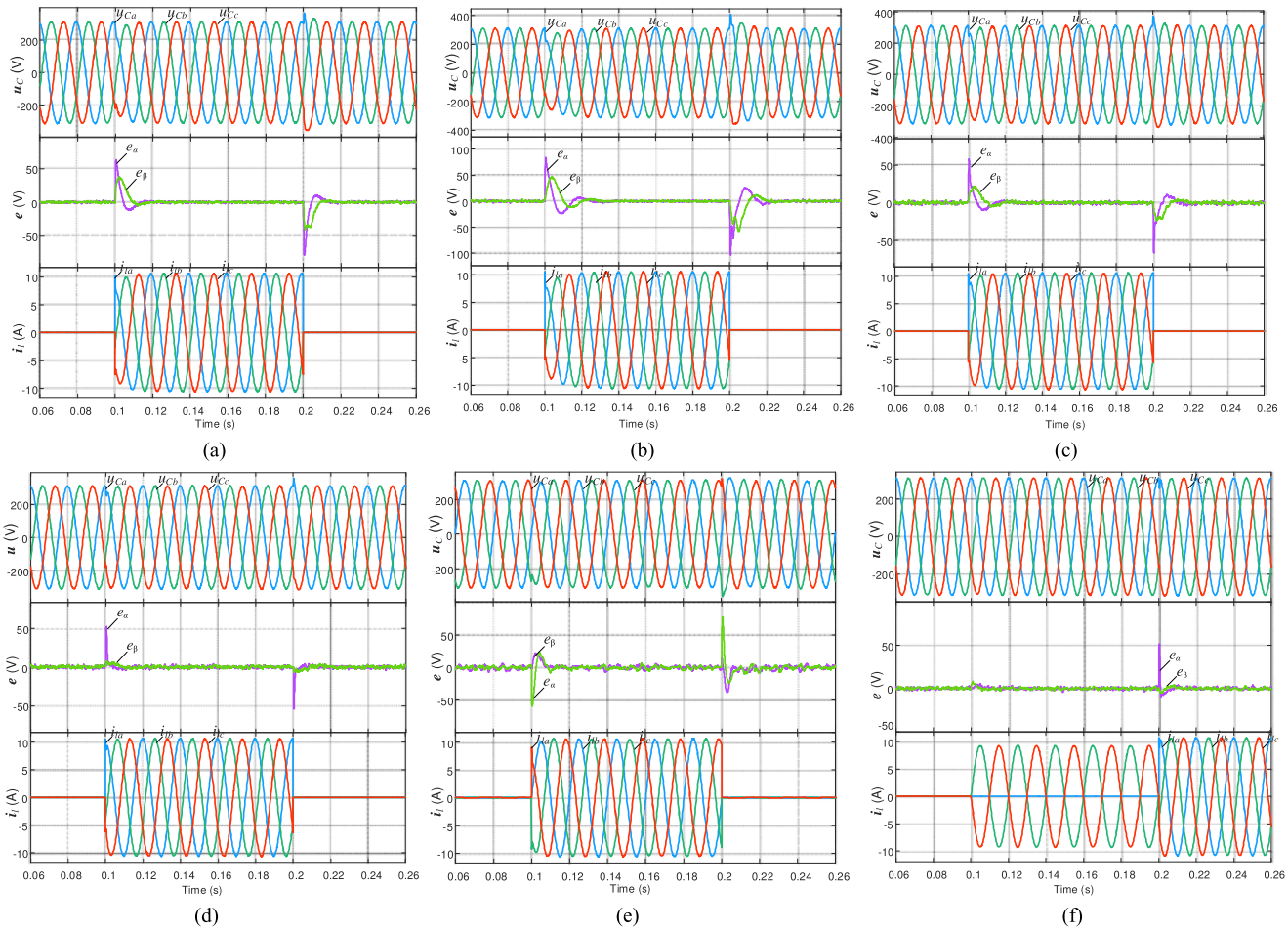

Fig. 8. Simulation results of: (a) optimal H_∞ control proposed in [20], (b) proposed LQR without load current decoupling, (c) proposed LQR with the optimal H_∞ load current decoupling, (d) proposed LQR with the zero-dynamic load current decoupling, (e) classical dual-loop control with load current decoupling when a 5-kW resistor load is connecting to the inverter, (f) proposed LQR with the zero-dynamic load current decoupling under unbalanced load.

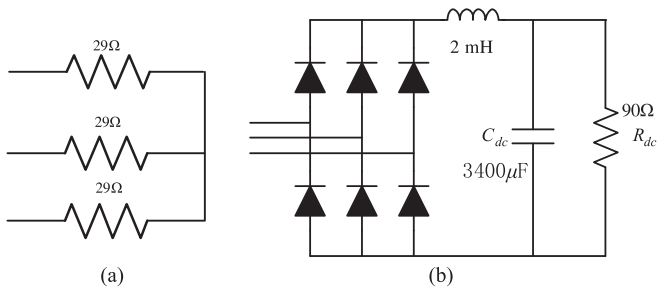

Fig. 9. Two kinds of loads: (a) linear and (b) nonlinear load circuit.

decoupling are 62.3 V and 14 ms, respectively. The corresponding waveforms are shown in Fig. 10(c). Still, the best transient performance is accomplished by the zero-dynamic decoupling control. As displayed in Fig. 10(d), the maximum voltage drop is 54.9 V and the dynamic recovering time is only about 6 ms. However, the error voltage has been substantially attenuated in a very short time of 1 ms, so that the output voltage waveforms have almost no variations to be observed.

The summarized transient performances and the advantages and disadvantages of the five controllers are compared in Table IV. Observing from the table, the experiment results are slightly different from the simulation results. Especially, the zero-dynamic experiment appears about 6 ms dynamic process. It is because of the uncertainties, such as the changing inductance. Nevertheless, the outcome of the zero-dynamic approach is still excellent.

B. Dynamic Performance of Inductance and Nonlinear loads

To test the dynamic response under different loads, the inductive and nonlinear loads are also suddenly connected to the inverter. The diode rectifier is adopted as it is a frequently used nonlinear load in industry and also adopted as the test nonlinear load in [11] and [12]. Fig. 11 shows the experiment results that demonstrate that the proposed algorithm is also valid under inductive and nonlinear loads. The dynamic responses are still excellent when the inductive and nonlinear loads are suddenly connected to the inverter.

C. Robustness Verification

In addition, the dynamic responses under nonnormal parameters are tested to verify the robustness analyzed in Section IV-B. As shown in Fig. 12, the dynamic response under 15 μF capacitance and 60 μF capacitance proves that the proposed

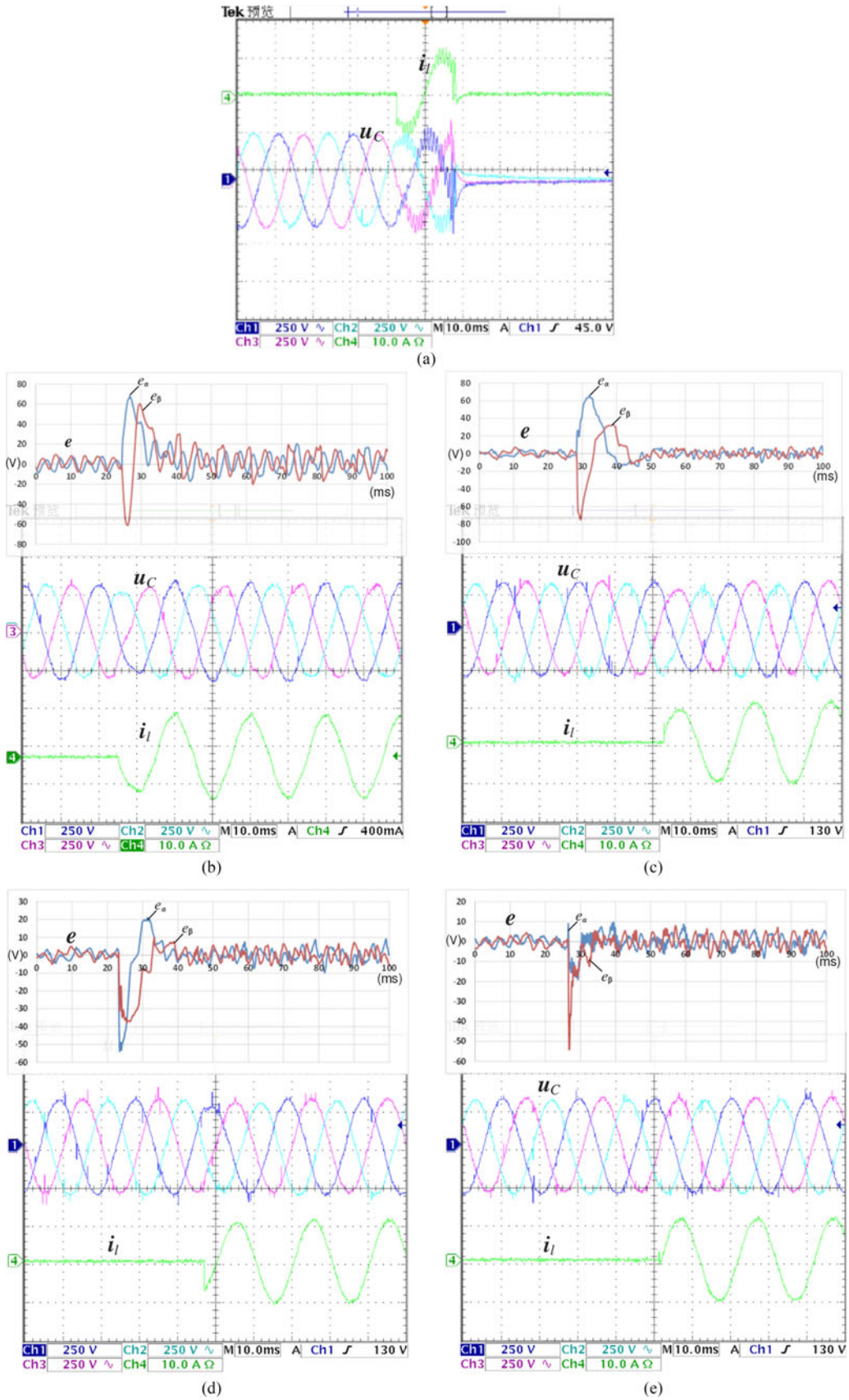

Fig. 10. Experiment results of: (a) optimal H_∞ control proposed in [20], (b) classical dual-loop control with load current decoupling, (c) LQR without load current decoupling, (d) LQR with the optimal H_∞ load current decoupling, (e) LQR with the zero-dynamic load current decoupling when the resistor load is connected to the inverter.

TABLE IV
DYNAMIC PERFORMANCE COMPARISON OF DIFFERENT CONTROLLERS

	The Optimal H_∞ Control Proposed in [20]		The LQR Without Load Current Decoupling		The Optimal H_∞ Load Current Decoupling		The Zero-Dynamic Load Decoupling		The Classical Dual-Loop Control	
	Voltage drop	Recovering time	Voltage drop	Recovering time	Voltage drop	Recovering time	Voltage drop	Recovering time	Voltage drop	Recovering time
Simulation	69 V	15 ms	83 V	22 ms	53 V	16 ms	51 V	0 ms	71 V	10
Experiment	Instable	Instable	83.7 V	20 ms	62.3 V	14 ms	54.9 V	6 ms	89 V	18
Advantages	Convenient optimal parameter design, small H_∞ norm leading to high disturbance-rejection ability		Convenient optimal parameter design, small feedback gains, high stability margins		Convenient optimal parameter design, small feedback gains, high stability margins, small H_∞ norm leading to high disturbance-rejection ability		Small feedback gains, fast dynamic response, high stability margins, high disturbance-rejection ability, low THD feeding loads, reduced number of *R* controllers		Explicit physical as guidance of control design.	
Disadvantages	Exorbitant feedback gains leading to instability, high THD feeding loads, slow dynamic response		Poor disturbance-rejection ability, high THD fee ding loads, slow dynamic response		Slow dynamic response		Root locus needed to determine the distribution of the configurable zeros		Lack of quantized optimal parameter design and adjustable load current decoupling control, cannot deal with the complex gains, slow dynamic response	

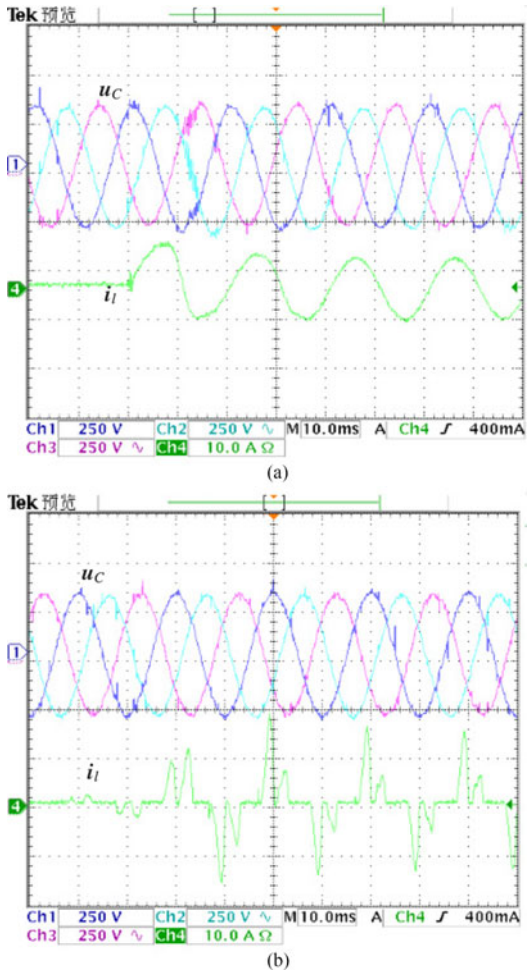

Fig. 11. Experimental dynamic response of the proposed zero-dynamic control when (a) 3-k Var inductive load and (b) nonlinear load shown in Fig. 9(b) are connected to the inverter.

zero-dynamic control has a strong robustness to the parameter uncertainties.

D. Steady-State Performance

In addition to the dynamic performance, the steady-state performance, for example, the THD, is also critical for the inverter voltage control. To study how the decoupling control and the DCVRC influence the THD index, a group of comparative experiments were performed. At first, single DCVRC control was performed with different decoupling strategies. Second, three DCVREs that contained fundamental positive sequence $(n = 1)$, fifth negative sequence $(n = -5)$, and seventh positive sequence $(n = 7)$ were adopted for the comparison. In this condition, the configurable zeros were located to eliminate the influence of fundamental positive sequence poles in zero-dynamic decoupling control, because they are dominated, and they are also the big concern for user. Furthermore, two kinds of loads, as shown in Fig. 9, were used for the test.

The monitored THD indices are summarized in Table V. As shown in Table V, horizontally the THD is reduced remarkably with the introduction of fifth and seventh DCVRCs especially for the nonlinear load. The harmonics in fifth- and seventh-order are essentially eliminated, which is the contribution of the fifth- and seventh-DCVRCs. Furthermore, vertically comparing, the THD is also decreased in a certain extent with the load current decoupling. This illustrates that the load current decoupling control is an efficient approach to decrease the THD.

In addition, the best THD indices, which are 0.3% and 1.2% in linear and nonlinear load, respectively, are achieved by the three DCVRCs with the zero-dynamic load current decoupling. The corresponding voltage waveforms are shown in Fig. 13. Limited by space, many other waveforms are omitted. Moreover, comparing to [23], only three controllers are employed to

TABLE V
THD COMPARISON

	One DCVRC (n = 1)		Three DCVRCs (n = 1, −5, 7)	
	linear load	nonlinear loads	linear load	nonlinear loads
The LQR without load current decoupling	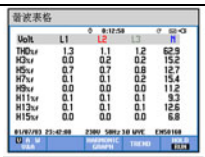	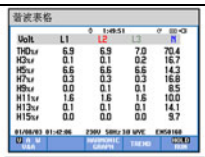		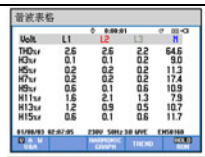
The optimal H_∞ load current decoupling	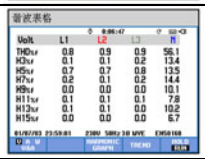			
The zero-dynamic load current decoupling				

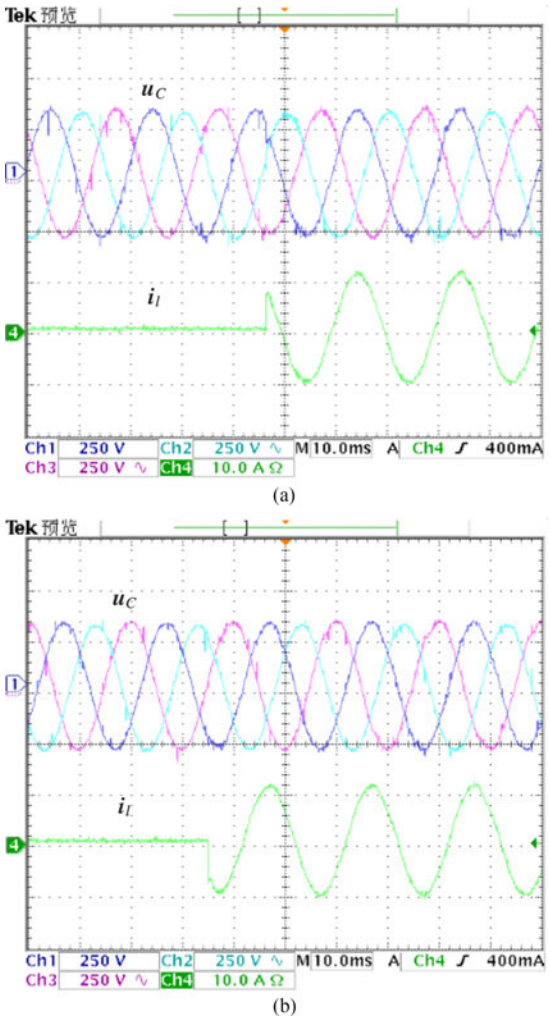

Fig. 12. Experimental dynamic response of the proposed zero-dynamic control under different parameters: (a) 15 μF capacitance and (b) 60 μF capacitance.

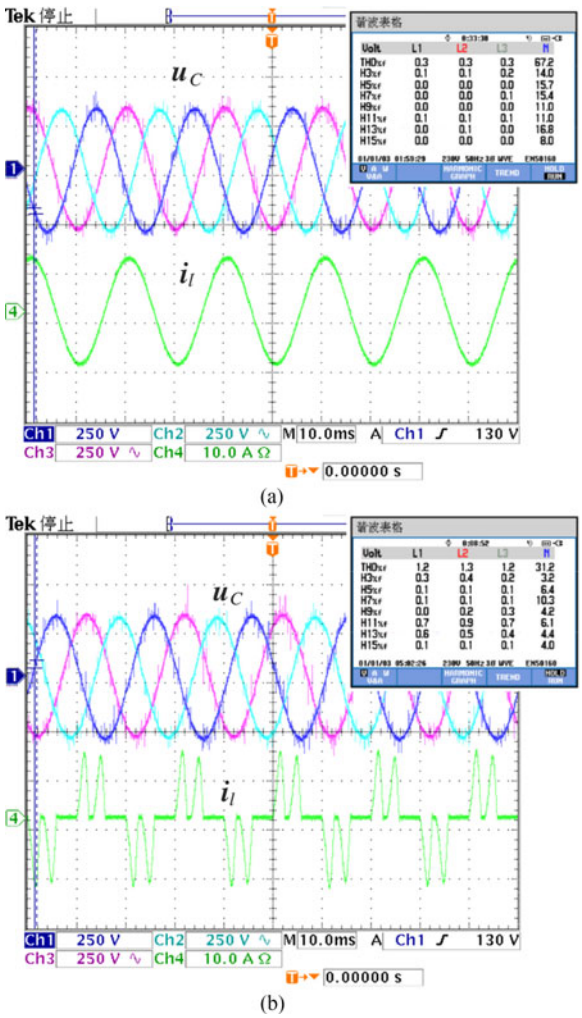

Fig. 13. Steady wave of the zero-dynamic decoupling control under: (a) linear resistor load and (b) nonlinear rectifier load.

achieve a preferable THD, it is the contribution of the proposed load current decoupling control.

VII. Conclusion

This paper has proposed a load current decoupling with the LQ state feedback control on an integrated α–β control structure for three-phase inverters. The approach supplies an effective disturbance decoupling design guideline for the state-space control structure applied to IMP-based controllers.

By means of the proposed optimal load current decoupling control, two merits are achieved. First of all, the excellent THD can be achieved by the reduced number of resonant controllers, which could efficiently release the design burden and control implementation weight in DSP. Second of all, thanks to the fast dynamic response achieved by the optimal load current decoupling control, the resonant controllers do not require high gains to acquire a fast dynamic response. Thus, the compromise between fast response and stability is not necessary when choosing the controller gains.

In summary, the steady state and dynamic performance are both improved by the proposed control approach. The disturbance-rejection ability is enhanced. The proposed approach also has a strong robustness despite parameter variations. In addition, thanks to the convenient extensibility of multiple controllers, the adoption of the static control gains and elimination of trial-and-error action for the control gains, the control method is practical and helpful for designers.

Appendix

A. Proof of (20)

Considering the following matrix inequality:

$$(\boldsymbol{A}-\boldsymbol{B}_1\boldsymbol{K}-q\boldsymbol{I})^T\boldsymbol{P}(\boldsymbol{A}-\boldsymbol{B}_1\boldsymbol{K}-q\boldsymbol{I})-r^2\boldsymbol{P}+\boldsymbol{Q}+\boldsymbol{K}^T\boldsymbol{R}\boldsymbol{K}<0 \tag{29}$$

then, it has

$$\left(\frac{\boldsymbol{A}-\boldsymbol{B}_1\boldsymbol{K}-q\boldsymbol{I}}{r}\right)^T\boldsymbol{P}\left(\frac{\boldsymbol{A}-\boldsymbol{B}_1\boldsymbol{K}-q\boldsymbol{I}}{r}\right)-\boldsymbol{P}<-\frac{\boldsymbol{Q}+\boldsymbol{K}^T\boldsymbol{R}\boldsymbol{K}}{r^2}<0 \tag{30}$$

which manifests that the system $(\boldsymbol{A}-\boldsymbol{B}_1\boldsymbol{K}-q\boldsymbol{I})/r$ is stable. Therefore, the poles of the system $(\boldsymbol{A}-\boldsymbol{B}_1\boldsymbol{K}-q\boldsymbol{I})/r$ are confined in the unit circle. Then, according to the linear system theory, the poles of the closed-loop system $\boldsymbol{A}-\boldsymbol{B}_1\boldsymbol{K}$ are restricted in disk $D(q, r)$.

Defining the Lyapunov function $V(\boldsymbol{x})=\boldsymbol{x}^T\boldsymbol{P}\boldsymbol{x}$. Then, considering two conditions: $q\geq 0, 0<q+r<1$ and $q<0, -1<q-r<0$, and according to Garcia [30] and Zhang *et al.* [31], it can be obtained that

$$(\boldsymbol{A}-\boldsymbol{B}_1\boldsymbol{K})^T\boldsymbol{P}(\boldsymbol{A}-\boldsymbol{B}_1\boldsymbol{K})-\boldsymbol{P}<-\left(\boldsymbol{Q}+\boldsymbol{K}^T\boldsymbol{R}\boldsymbol{K}\right)<0. \tag{31}$$

Then, considering discrete-time difference $\Delta V(\boldsymbol{x}_k)=\boldsymbol{x}_k^T[(\boldsymbol{A}-\boldsymbol{B}_1\boldsymbol{K})^T\boldsymbol{P}(\boldsymbol{A}-\boldsymbol{B}_1\boldsymbol{K})-\boldsymbol{P}]\boldsymbol{x}_k<0$, the Lyapunov function is monotonously convergent into zero, and $V(\boldsymbol{x}_k)\leq V(\boldsymbol{x}_0)=\boldsymbol{x}_0^{\mathrm{T}}\boldsymbol{P}x_0$. Furthermore, from (31), it yields

$$\begin{aligned}J&=\sum_{k=0}^{\infty}\left(\boldsymbol{x}_k^T\boldsymbol{Q}\boldsymbol{x}_k+\boldsymbol{u}_k^T\boldsymbol{R}\boldsymbol{u}_k\right)=\sum_{k=0}^{\infty}\left(\boldsymbol{x}_k^T\left(\boldsymbol{Q}+\boldsymbol{K}^T\boldsymbol{R}\boldsymbol{K}\right)\boldsymbol{x}_k\right)\\&<-\sum_{k=0}^{\infty}\Delta V(\boldsymbol{x}_k)=V(\boldsymbol{x}_0)=\boldsymbol{x}_0^T\boldsymbol{P}\boldsymbol{x}_0=\boldsymbol{x}_0^T\boldsymbol{W}^{-1}\boldsymbol{x}_0.\end{aligned} \tag{32}$$

At last, according to (29), the flowing equivalent LMI is derived:

$$\begin{bmatrix}-r^2\boldsymbol{P} & (\boldsymbol{A}-\boldsymbol{B}_1\boldsymbol{K}-q\boldsymbol{I})^T & \boldsymbol{I} & \boldsymbol{K}^T\\ (\boldsymbol{A}-\boldsymbol{B}_1\boldsymbol{K}-q\boldsymbol{I}) & -\boldsymbol{P} & & \\ \boldsymbol{I} & & -\boldsymbol{Q}^{-1} & \\ \boldsymbol{K} & & & -\boldsymbol{R}^{-1}\end{bmatrix}<0. \tag{33}$$

Pre- and post-multiplying the above inequality by diag([$\boldsymbol{P}^{-1}, \boldsymbol{I}, \boldsymbol{I}, \boldsymbol{I}$]) and defining $\boldsymbol{W}=\boldsymbol{P}^{-1}, \boldsymbol{V}=\boldsymbol{K}\boldsymbol{P}^{-1}=\boldsymbol{K}\boldsymbol{W}$, (20) is derived.

B. Proof of (25) and (26)

Based on the Schur complement, (23) becomes

$$\begin{bmatrix}-\boldsymbol{P} & & (\boldsymbol{A}-\boldsymbol{B}_1\boldsymbol{K})^T & \boldsymbol{C}^T\\ & -\gamma^2\boldsymbol{I} & (\boldsymbol{B}_2+\boldsymbol{B}_1\boldsymbol{K}_d)^T & \\ (\boldsymbol{A}-\boldsymbol{B}_1\boldsymbol{K}) & \boldsymbol{B}_2+\boldsymbol{B}_1\boldsymbol{K}_d & -\boldsymbol{P}^{-1} & \\ \boldsymbol{C} & & & -\boldsymbol{I}\end{bmatrix}<0. \tag{34}$$

Pre- and post-multiplying (34) by diag([$\boldsymbol{P}^{-1}, \boldsymbol{I}, \boldsymbol{I}, \boldsymbol{I}$]), where diag() denotes the diagonal matrix, (34) translates into the following:

$$\begin{bmatrix}-\boldsymbol{P}^{-1} & & (\boldsymbol{A}-\boldsymbol{B}_1\boldsymbol{K}\boldsymbol{P}^{-1})^T & (\boldsymbol{C}\boldsymbol{P}^{-1})^T\\ & -\gamma^2\boldsymbol{I} & (\boldsymbol{B}_2+\boldsymbol{B}_1\boldsymbol{K}_d)^T & \\ (\boldsymbol{A}-\boldsymbol{B}_1\boldsymbol{K}\boldsymbol{P}^{-1}) & \boldsymbol{B}_2+\boldsymbol{B}_1\boldsymbol{K}_d & -\boldsymbol{P}^{-1} & \\ \boldsymbol{C}\boldsymbol{P}^{-1} & & & -\boldsymbol{I}\end{bmatrix}<0. \tag{35}$$

Then, defining $\boldsymbol{W}=\boldsymbol{P}^{-1}$, $\rho=\gamma^2$, the optimization problem (25) and (26) can be constructed.

References

[1] J. Rocabert, A. Luna, F. Blaabjerg, and P. Rodríguez, "Control of power converters in AC microgrids," *IEEE Trans. Power Electron.*, vol. 27, no. 11, pp. 4734–4749, Nov. 2012.

[2] A. M. Bouzid, J. M. Guerrero, A. Cheriti, M. Bouhamida, P. Sicard, and M. Benghanem, "A survey on control of electric power distributed generation systems for microgrid applications," *Renewable Sustain. Energy Rev.*, vol. 44, pp. 751–766, Jan. 2015.

[3] P. C. Loh, M. J. Newman, D. N. Zmood, and D. G. Holmes, "A comparative analysis of multiloop voltage regulation strategies for single and three-phase UPS systems," *IEEE Trans. Power Electron.*, vol. 18, no. 5, pp. 1176–1185, Sep. 2003.

[4] Y. A. R. I. Mohamed and A. Radwan, "Hierarchical control system for robust microgrid operation and seamless mode transfer in active distribution systems," *IEEE Trans. Smart Grid*, vol. 2, no. 2, pp. 352–362, Jun. 2011.
[5] R. Razi and M. Monfared, "Simple control scheme for single-phase uninterruptible power supply inverters with Kalman filter-based estimation of the output voltage," *IET Power Electron.*, vol. 8, no. 9, pp. 1817–1824, Apr. 2015.
[6] F. de Bosio, L. A. Ribeiro, F. D. Freijedo, M. Pastorelli, and J. M. Guerrero "Effect of state feedback coupling and system delays on the transient performance of stand-alone VSI with LC output filter," *IEEE Trans. Ind. Electron.*, vol. 63, no. 8, pp. 4909–4918, Aug. 2016.
[7] G. Escobar, A. A. Valdez, J. Leyva-Ramos, and P. Mattavelli, "Repetitive-based controller for a UPS inverter to compensate unbalance and harmonic distortion," *IEEE Trans. Ind. Electron*, vol. 54, no. 1, pp. 504–510, Feb. 2007.
[8] H. Deng, R. Oruganti, and D. Srinivasan, "A simple control method for high-performance UPS inverters through output-impedance reduction," *IEEE Trans. Ind. Electron.*, vol. 55, no. 2, pp. 888–898, Feb. 2008.
[9] P. Cortés, G. Ortiz, J. I. Yuz, J. Rodríguez, S. Vazquez, and L. G. Franquelo, "Model predictive control of an inverter with output LC filter for UPS applications," *IEEE Trans. Ind. Electron.*, vol. 56, no. 6, pp. 1875–1883, Feb. 2009.
[10] V. Yaramasu, M. R. Ivera, M. Narimani, B. Wuet, and J. Rodriguez, "Model predictive approach for a simple and effective load voltage control of four-leg inverter with an output filter," *IEEE Trans. Ind. Electron.*, vol. 61, no. 10, pp. 5259–5270, Oct. 2014.
[11] T. D. Do, V. Q. Leu, Y. S. Choi, H. H. Choiet, and J. Jung, "An adaptive voltage control strategy of three-phase inverter for stand-alone distributed generation systems," *IEEE Trans. Ind. Electron.*, vol. 60, no. 12, pp. 5660–5672, Oct. 2013.
[12] E. K. Kim, F. Mwasilu, H. H. Choi, and J. W. Jung, "An observer-based optimal voltage control scheme for three-phase UPS systems," *IEEE Trans. Ind. Electron.*, vol. 62, no. 4, pp. 2073–2081, Apr. 2015.
[13] J. W. Jung, N. T. Vu, T. D. Q. Dang, T. D. Doet, Y. Choi, and H. H. Choi, "A three-phase inverter for a standalone distributed generation system: Adaptive voltage control design and stability analysis," *IEEE Trans. Energy Convers.*, vol. 29, no. 1, pp. 46–56, Mar. 2014.
[14] H. Komurcugil, N. Altin, S. Ozdemir, and I. Sefa, "An extended Lyapunov-function-based control strategy for single-phase UPS inverters," *IEEE Trans. Power Electron.*, vol. 30, no. 7, pp. 3976–3983, Jul. 2015.
[15] D. E. Kim and D. C. Lee, "Feedback linearization control of three-phase UPS inverter systems," *IEEE Trans. Ind. Electron.*, vol. 57, no. 3, pp. 963–968, Mar. 2010.
[16] A. Houari, H. Renaudineau, J. P. Martin, S. Pierfederici, and F. Meibody-Tabar, "Flatness-based control of three-phase inverter with output filter," *IEEE Trans. Ind. Electron.*, vol. 59, no. 7, pp. 2890–2897, Jul. 2012.
[17] J. S. Lim and Y. I. Lee, "Design of a robust controller for three-phase UPS systems using LMI approach," in *Proc. Int. Symp. Power Electron. Power Electron., Elect. Drives. Autom. Motion*. 2012, pp. 654–657.
[18] J. S. Lim, C. Park, J. Han, and Y. I. Lee, "Robust tracking control of a three-phase DC–AC inverter for UPS applications," *IEEE Trans. Ind. Electron.*, vol. 61, no. 8, pp. 4142–4151, Aug. 2014.
[19] G. Willmann, D. F. Coutinho, L. F. A. Pereira, and F. B. Líbano, "Multiple-loop H-infinity control design for uninterruptible power supplies," *IEEE Trans. Ind. Electron.*, vol. 54, no. 3, pp. 1591–1602, Jun. 2012.
[20] L. F. Alves Pereira, J. Vieira Flores, G. Bonan, and J. M. Gomes da Silva, Jr, "Multiple resonant controllers for uninterruptible power supplies—A systematic robust control design approach," *IEEE Trans. Ind. Electron.*, vol. 61, no. 3, pp. 1528–1538, Mar. 2014.
[21] A. Hasanzadeh, C. S. Edrington, B. Maghsoudlou, and H. Mokhtari, "Optimal LQR-based multi-loop linear control strategy for UPS inverter applications using resonant controller," in *Proc. IEEE 50th Decis. Control. Eur. Control Conf.*, 2011, pp. 3080–3085.
[22] A. Hasanzadeh, C. S. Edrington, B. Maghsoudlou, F. Fleming, and H. Mokhtari, "Multi-loop linear resonant voltage source inverter controller design for distorted loads using the linear quadratic regulator method," *IET Power Electron.*, vol. 5, no. 6, pp. 841–851, Mar. 2012.
[23] X. Quan, X. Dou, Z. Wu, Z. Wu. M. Hu, and J.Yuan, "Harmonic voltage resonant compensation control of a three-phase inverter for battery energy storage systems applied in isolated microgrid," *Elect. Power Sys. Res*, vol. 131, pp. 205–217, 2016.
[24] A. Kaszewski, L. M. Grzesiak, and B. Ufnalski, "Multi-oscillatory LQR for a three-phase four-wire inverter with L3nC output filter," in *Proc. Annu. Conf. Ind. Electron. Soc.*, 2012, pp. 3449–3455.
[25] B. Ufnalski, A. Kaszewski, and L. M. Grzesiak, "Particle swarm optimization of the multioscillatory LQR for a three-phase four-wire voltage-source inverter with an output filter," *IEEE Trans. Ind. Electron.*, vol. 62, no. 1, pp. 484–493, Jan. 2015.
[26] A. Kaszewski, B. Ufnalski, and L. M. Grzesiak, "An LQ controller with disturbance feedforward for the 3-phase 4-leg true sine wave inverter," in *Proc. IEEE Int. Conf. Ind. Technol.*, Cape Town, South Africa, 2013, pp. 1924–1930.
[27] C. Scherer, "H∞ control by state feedback: An iterative algorithm and characterization of high-gain occurence," *Syst. Control Lett.*, vol. 12, no. 5, pp. 383–391, Jun. 1989.
[28] B. D. O. Anderson and J. B. Moore, *Optimal Control: Linear Quadratic Methods*. Sydney, Australia: Prentice-Hall, 1990.
[29] C. A. Busada, S. G. Jorge, A. E. Leon, and J. A. Solsona, "Current controller based on reduced order generalized integrators for distributed generation systems," *IEEE Trans. Ind. Electron.*, vol. 59, no. 7, pp. 2898–2909, Jul. 2012.
[30] G. Garcia, "Quadratic guaranteed cost and disc pole location control for discrete-time uncertain systems," *IEE Proc. Control Theory Appl.*, vol. 144, no. 6, pp. 545–548, Nov. 1997.
[31] D. Zhang *et al.*, "Satisfactory reliable H∞ guaranteed cost control with D-stability and control input constraints," *IET Control Theory Appl.*, vol. 2, no. 8, pp. 643–653, 2008.
[32] P. Youngjin, "Robust H∞ control for linear discrete-time systems with norm-bounded nonlinear uncertainties," *IEEE Trans. Automat. Control*, vol. 48, no. 8, pp. 1469–1470, Aug. 2003.

Xiangjun Quan (S'16) received the B.S.E.E. and the M.S. degrees in power systems and its automation from Chongqing University, Chongqing, China, in 2007 and Southeast University, Nanjing, China, in 2014, where he is currently working toward the Ph.D. degree with major of Electrical Engineering. He is also studying in FREEDM Systems Center at NC State University as exchanging student from Feb. 2017.

His current research interests include digital control technique, renewable energy generation systems and microgrid.

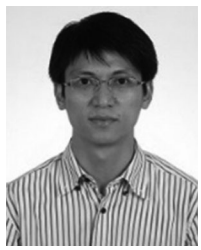

Zaijun Wu received the B.Eng. degree in power system and its automation from the Hefei University of Technology, Hefei, China, in 1996, and the Ph.D. degree in electrical engineering from Southeast University, Nanjing, China, in 2004.

He was a Visiting Scholar at the Ohio State University, USA, from 2012 to 2013. He is currently a Professor in the School of Electrical Engineering, Southeast University. His research interests include substation automation, microgrid, and power quality. He is the author or coauthor of about 60 referred journal papers, and a reviewer of several journals.

Xiaobo Dou received the B.S.E.E. degree from Ho-Hai University, Nanjing, China, in 2001, and the Ph.D. degree in electrical engineering from Southeast University, Nanjing, China, in 2006.

He has been an Associate Professor at Southeast University since September 2009. His current interests include smart grid, microgrid, and renewable energy resources.

Minqiang Hu received the Ph.D. degree in electrical engineering from the Huazhong University of Science and Technology, Wuhan, China, in 1990.

He is currently a Full Professor in the School of Electrical Engineering, Southeast University, Nanjing, China. His research interests include electric machine modeling and simulation, protection and control and substation power quality monitoring.

Alex Q. Huang (S'91–M'94–SM'96–F'05) received the B.Sc. degree from Zhejiang University, Hangzhou, China, in 1983, the M.Sc. degree from the Chengdu Institute of Radio Engineering, Chengdu, China in 1986, both in electrical engineering and the Ph.D. degree from Cambridge University, Cambridge, U.K., in 1992.

From 1994 to 2004, he was a Professor at CPES Virginia Tech. From 2004 to 2017, he was with the North Carolina State University as the Progress Energy Distinguished Professor of Electrical and Computer Engineering. In September 2017, he will join the University of Texas at Austin, Austin, TX, USA, as the Dula D. Cockrell Centential Chair in Engineering. At North Carolina State, he established the FREEDM Systems Center in 2008 and the PowerAmerica Institute in 2014. He has mentored more than 80 Ph.D. and master students to graduation, and has published more than 500 papers in journals and conferences. His current research interests include WBG power semiconductor devices, high density power converters, medium-voltage power converters, and renewable energy systems.

Dr. Huang has been granted more than 20 U.S. patents. He has received the NSF CAREER Award, the prestigious R & D 100 Award, and the MIT Technology Review's 2011 Technology of the Year Award.